RSC Advances

PAPER

Cite this: *RSC Adv.*, 2024, **14**, 24335

Ultra small gold nanoclusters supported on two-dimensional bismuth selenium nanosheets for synergistic photothermal and photodynamic tumor therapy†

Chenxi Li,‡[ab] Xueyang Fang,‡*[b] Qingdong Zeng,[ab] Li Zeng,*[b] Bin Zhang *[b] and Guohui Nie*[b]

Two-dimensional (2D) bismuth selenium (Bi_2Se_3) nanosheets have exceptional surface area and superior surface modification capabilities, facilitating the effective loading of nanoprobes, metal particles, and other substances. Additionally, thiolated ultrasmall gold nanoclusters (Au NCs), distinguished by their high photoluminescent activity and modulatable surface charges, enable efficient loading onto the 2D Bi_2Se_3 surfaces. In this study, we successfully prepared Bi_2Se_3 nanosheets by sonication-assisted liquid phase exfoliation and loaded Au clusters on their surface through an amide bond reaction. The loading of Au NCs significantly augments the photothermal and photocatalytic capabilities of Bi_2Se_3 nanosheets and exhibits obvious anti-cancer therapeutic effects through *in vitro* and *in vivo* experiments. In summary, the as-prepared AuNC@Bi_2Se_3 nanocomposites showed combined near-infrared light-initiated photothermal/photodynamic therapy (PTT/PDT) against tumors, demonstrating their potential as novel theranostic agents for biomedical applications.

Received 28th April 2024
Accepted 26th July 2024

DOI: 10.1039/d4ra03142c

rsc.li/rsc-advances

1. Introduction

Cancer poses a significant threat to human health, due to its high incidence and mortality rates. Traditional therapeutic modalities, such as radiation and chemotherapy, frequently result in adverse body damage and undesirable side effects.[1,2] In recent years, a growing body of research has focused on light-triggered therapeutic strategies against cancer based on nanomaterials.[3–5] Near-infrared (NIR) light-triggered therapeutic strategies, including photothermal therapy (PTT) and photodynamic therapy (PDT), can destroy tumor cells through local high temperature or *in situ* generation of reactive oxygen species (ROS).[6–8] These methods are particularly appealing due to their minimal systemic toxicity, non-invasive nature, and high selectivity towards cancer cells. PTT refers to the process where photothermal agents (PTAs) concentrated at the tumor site generate local high temperatures under the irradiation of an NIR laser, effectively targeting and eliminating tumor cells.[9–11] Hence, the efficacy of PTT hinges on the photothermal conversion efficiency (PTCE) of the PTAs.[12] PDT entails the generation of cytotoxic reactive oxygen species (ROS), including hydroxyl radicals ($^{\bullet}OH$), singlet oxygen ($^1O_2$), and superoxide radicals ($^{\bullet}O_2^-$), by irradiating photosensitizers (PSs) located in tumor tissues with an NIR laser.[13,14] A substantial accumulation of cytotoxic ROS in tumor regions can initiate intracellular mitochondrial apoptosis or stimulate immune responses, ultimately destroying tumor cells.[15–17] The synergistic treatment of PTT and PDT can improve the therapeutic effect and maximize the anti-tumor effect of nanomaterials without increasing drug toxicity to surrounding normal tissues, which is conducive to the healthy recovery of patients.

Recently, noble metal nanoparticles (NMNPs) have garnered significant attention in the field of biomedicine. Under the influence of laser irradiation, NMNPs can facilitate temperature increase predominantly *via* the localized surface plasmon resonance (LSPR) mechanism. LSPR refers to the phenomenon of collective oscillations of free electrons on the surface of metallic particles or nanostructures upon light excitation. This phenomenon can lead to thermal dissipation through radiative processes, resulting in localized heating and electromagnetic field amplification proximate to the particles. Alternatively, it may generate hot carriers, such as electrons and holes, through non-radiative mechanisms. These characteristics offer the potential for augmenting the photothermal responsiveness and

[a]*Graduate Collaborative Training Base of Shenzhen Second People's Hospital, Heng Yang Medical School, University of South China, Hengyang, Hunan, 421001, China*
[b]*Shenzhen Key Laboratory of Nanozymes and Translational Cancer Research, Institute of Translational Medicine Department of Otolaryngology Shenzhen Second People's Hospital, The First Affiliated Hospital of Shenzhen University, Health Science Center, Shenzhen 518035, China. E-mail: binzhang@email.szu.edu.cn; nieguohui@email.szu.edu.cn; FANGXueyang0210@163.com*

† Electronic supplementary information (ESI) available. See DOI: https://doi.org/10.1039/d4ra03142c

‡ Chenxi Li and Xueyang Fang contributed equally to this work.

photocatalytic efficiency of nanomaterials. For instance, Yuan *et al.* used the sodium hydroxide-mediated reduction of sodium borohydride to successfully synthesize glutathione-protected Au nanoclusters (NCs) with excellent catalytic effects.[18] These Au NCs are suitable for heterogeneous catalysis due to their relatively large surface area and abundant active centers. However, the stability of NMNPs is a critical issue, as they are unstable under laser irradiation due to their high surface energy, which can lead to a decrease or disappearance of the photocatalytic effect.[19–22] Two-dimensional (2D) nanomaterials with superior physicochemical characteristics have emerged as the optimal choice for maintaining the stability of these cluster vectors.[23] And when certain NMNPs are loaded onto the surface of 2D nanomaterials, they can achieve enhanced photothermal and photocatalytic abilities.[24–26] As an illustration, the extensive surface area of the 2D bismuth selenium (Bi_2Se_3) nanosheets can offer ample space for NMNPs loading. It has been demonstrated that selenium is an essential trace element in the human body and Bi_2Se_3 nanosheets can release a certain amount of selenium in the physiological environment, which can effectively prevent the incidence of cancer, inflammation, and cardiovascular diseases.[27,28] What's more, Bi_2Se_3 nanosheets have shown promise as superior photothermal conversion agents according to their light absorption coefficient and they can generate plenty of ROS under light irradiation due to their narrow band gap.[29,30] In 2017, Song *et al.* used ultra-thin Bi_2Se_3 nanosheets for targeted cancer therapy, achieving promising therapeutic effects.[31]

In this study, we construct rationally designed 2D AuNC@Bi_2Se_3 nanocomposites for effective photothermal–photodynamic synthetic tumor therapy (Fig. 1). Bi_2Se_3 nanosheets were modified with chitosan (CS) to improve stability. Then, Au NCs were covalently bound to CS-stabilized Bi_2Se_3 nanosheets through amido bond, enhancing their photothermal and photodynamic efficiency. Under 808 nm NIR laser irradiation, AuNC@Bi_2Se_3 nanocomposites can exhibit good photothermal efficacy and catalyze the excess hydrogen peroxide (H_2O_2) in the tumor microenvironment (TME) for the production of $^{\bullet}O_2^-$ to trigger PDT. *In vitro* and *in vivo* antitumor experiments performed under laser irradiation showed superior tumor-suppressing effects. This study develops a new nanoplatform tailored for PDT/PTT synergistic cancer therapy.

2. Materials and methods

2.1 Materials

Powder of Bi_2Se_3 was purchased from Beijing Yan Nuo Xin Cheng Technology Company. CS, NaOH, and MPA were obtained from Maclin Company. All other solvents and chemicals were acquired from Sinopharm Chemical Reagent Co., Ltd. All the items used for cell culture were purchased from Thermo Fisher Scientific Corporation.

2.2 Synthesis of 2D Bi_2Se_3

Firstly, chitosan powder (0.8 mg ml^{-1}) was dissolved in a 5% acetic acid liquor to prepare a chitosan solution. Bi_2Se_3 powder (10 mg ml^{-1}) was then dissolved in the chitosan solution and exfoliated using sonication in 4 °C ice water for two hours. Following this, the supernatant was collected by centrifugation at 1500 rpm for 30 minutes. This process was repeated approximately six times to obtain more Bi_2Se_3 nanosheets supernatant. Finally, the ultrathin CS-modified Bi_2Se_3 nanosheets (Bi_2Se_3@CS) were obtained from the precipitate by centrifugation at 12 000 rpm for 20 minutes.

2.3 Synthesis of AuNC@Bi_2Se_3 nanocomposite

Au NCs were synthesized as reported.[21] These clusters were then added to the Bi_2Se_3 nanosheets solution and stirred with NHS and EDC for 12 h. Following this, the pure AuNC@Bi_2Se_3 nanocomposites were acquired by dialysis for 24 h.

2.4 Characterizations of AuNC@Bi_2Se_3

The TEM (Thermo Fisher) was utilized to verify the morphology and structure of AuNC@Bi_2Se_3. Particle size analysis and zeta potential of the nanocomplex were characterized using a Linessizer 500 (Anton Paar GmbH). Additionally, (X-ray photoelectron spectroscopy) XPS was employed to verify the structure and chemical characteristics.

2.5 Photothermal effects

For the measurement of photothermal performance, UV-vis spectroscopy (Thermo Fisher) was used to verify the absorption ability of AuNC@Bi_2Se_3 nanocomposites with varying concentrations (0 ppm, 3.125 ppm, 6.25 ppm, 12.5 ppm, 25 ppm, 50 ppm). AuNC@Bi_2Se_3 nanocomposites (25 ppm) were irradiated under NIR laser with different power densities (0.5, 0.75, 1.0, 1.25, and 1.5 W cm^{-2}, 6 min). Additionally, AuNC@Bi_2Se_3 nanocomposites with various concentrations (0 ppm, 3.125 ppm, 6.25 ppm, 12.5 ppm, 25 ppm, 50 ppm) were irradiated by NIR laser (808 nm, 1 W cm^{-2}). What's more, the AuNC@Bi_2Se_3 aqueous solution (25 ppm) was irradiated by NIR laser (808 nm, 1 W cm^{-2}) until reaching its maximum temperature, then naturally decreased to room temperature to measure its photothermal stability. This cycle was repeated three times, and an infrared thermal camera (FLIR) was used to record these temperature changes. The PTCE (η) of the AuNC@Bi_2Se_3 nanocomposites was calculated based on these temperature changes.

2.6 Detection of superoxide radicals ($^{\bullet}O_2^-$)

Electron spin resonance (ESR) was employed to confirm the production of $^{\bullet}O_2^-$. The dihydrorhodamine 123 (DHR123) assay can detect the production of $^{\bullet}O_2^-$ through a colorimetric reaction and the fluorescence generated in this reaction can be excited at 530 nm.[14,32] The DHR123 simulating solution comprised 100 ppm DHR, 100 ppm H_2O_2, and 10 ppm AuNC@Bi_2Se_3. These mixed solutions were irradiated under 808 nm laser, with a power density of 1 W cm^{-2}, for 5 minutes. The optical density was observed using a multimode microplate reader.

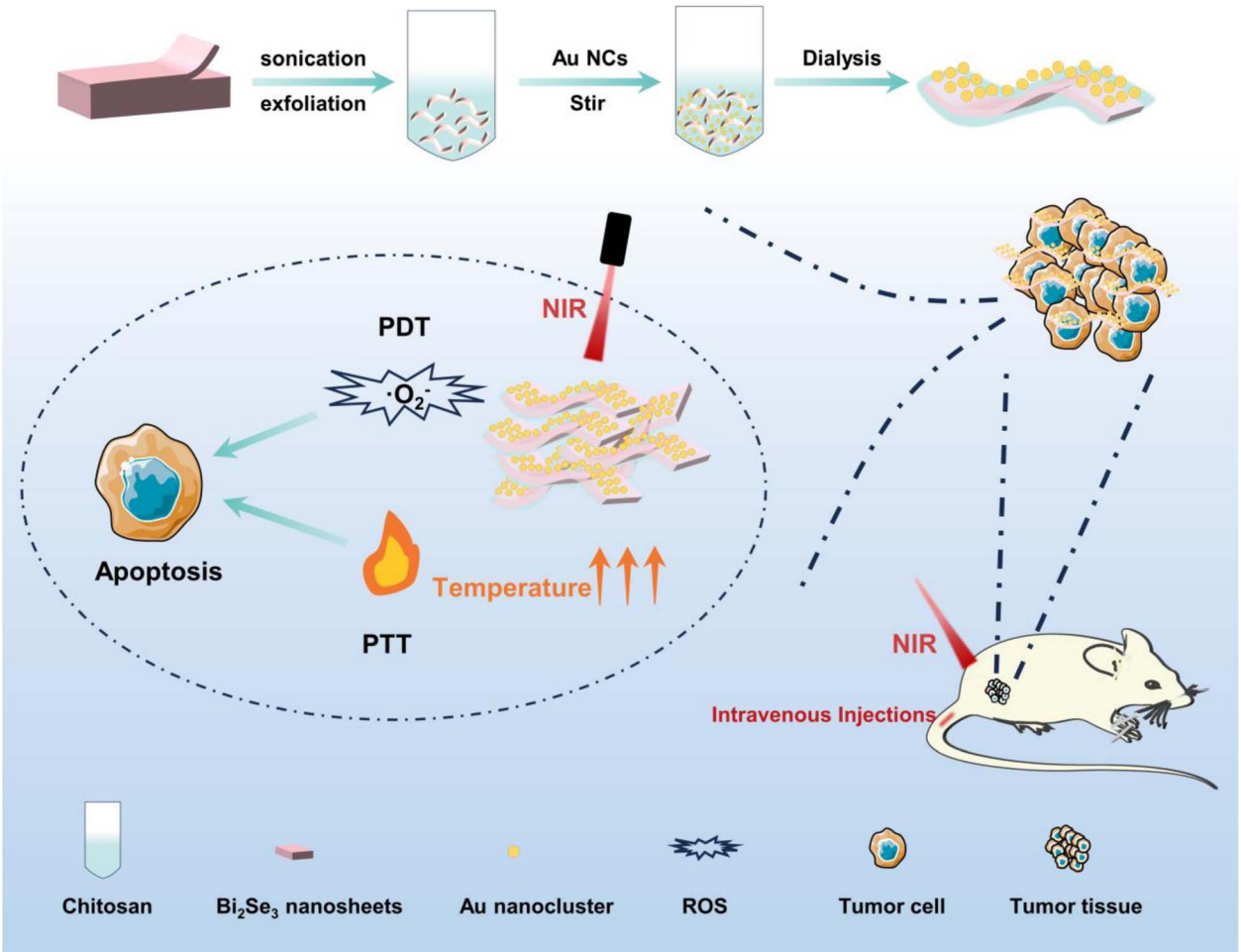

Fig. 1 Illustration of the synthesis of AuNC@Bi_2Se_3 nanocomposites and its synthetic photothermal/photodynamic therapy (PTT/PDT) in tumor microenvironment (TME).

2.7 Cytotoxicity experiment

4T1 cells were seeded in a 96-well plate for 12 h with 1×10^4 cells per well and then incubated with varying concentrations of Bi_2Se_3 and AuNC@Bi_2Se_3 (0 ppm, 5 ppm, 10 ppm, 15 ppm, 20 ppm, 25 ppm), respectively. After a 4 h incubation, NIR laser irradiation (808 nm, 1 W cm^{-2}) was conducted for 5 minutes, followed by treatment with CCK8 solution for 2 h the next day.[33] The results at 450 nm were then observed using a multifunctional microplate reader.

2.8 *In vitro* ROS detection

To detect the generation of ROS *in vitro*, 4T1 cells treated with four different groups (PBS, PBS + laser, AuNC@Bi_2Se_3, AuNC@Bi_2Se_3 + laser) were stained with 2′,7′-dichlorodihydrofluorescein diacetate (DCFH-DA) and DHE (AuNC@Bi_2Se_3 concentration: 12.5 ppm; laser: 808 nm, 1 W cm^{-2}, 5 min), respectively. After 30 minutes of incubation, DCFH-DA formed a green fluorescent substance (DCF), and DHE exhibited red fluorescence. The intracellular fluorescence was captured by an Echo Hybrid Microscope.

2.9 AM/PI

4T1 cells were seeded in a 12-well plate at 1×10^5 cells per well and incubated for 12 h. After 4 h incubation with various groups (PBS, PBS + laser, Bi_2Se_3, Bi_2Se_3 + laser, AuNC@Bi_2Se_3, AuNC@Bi_2Se_3 + laser), the cells were irradiated with an 808 nm laser (1 W cm^{-2}) for 5 min. Subsequently, calcein AM and propidium iodide (AM/PI) were added to form different fluorescent substances in living and dead cells after 30 minutes of incubation. The intracellular fluorescence of the stained cells was observed using an Echo Hybrid Microscope.

2.10 Apoptosis analysis

4T1 cells were seeded in a 6-well plate at a density of 1.5×10^5 cells per well, and incubated for 12 h. Following 4 h incubation of different groups, including PBS, PBS + laser, Bi_2Se_3, Bi_2Se_3 + laser, AuNC@Bi_2Se_3, and AuNC@Bi_2Se_3 + laser, 4T1 cells were irradiated by an 808 nm laser (1 W cm^{-2}) for 5 minutes. Subsequently, in 4 h incubation, the cells were stained with annexin V-fluorescein isothiocyanate/propidium iodide (annexin V-FITC/PI). The rate of cell apoptosis was quantified by flow cytometry analysis.

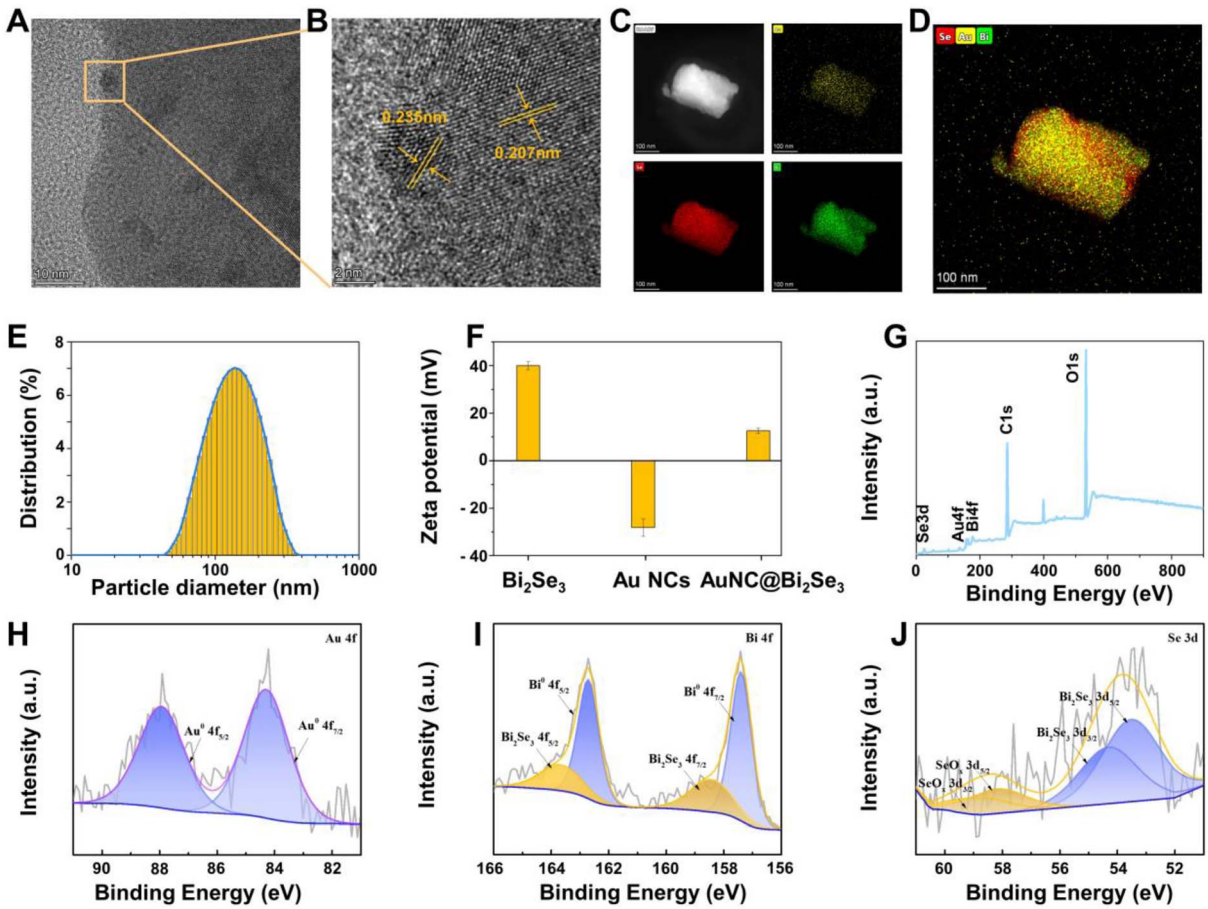

Fig. 2 (A) Representative TEM image of AuNC@Bi_2Se_3. (B) HRTEM image of AuNC@Bi_2Se_3. (C and D) HAADF-STEM image of AuNC@Bi_2Se_3 nanocomposites and its corresponding elemental mapping. (E) DLS measurement of AuNC@Bi_2Se_3. (F) Zeta potential changes of Bi_2Se_3, AuNC and AuNC@Bi_2Se_3. (G) XPS spectrum of AuNC@Bi_2Se_3. (H–J) High-resolution XPS spectrum of Au 4f, Bi 4f and Se 3d electrons.

2.11 *In vivo* therapeutic

1×10^6 4T1 cells (100 μl) suspension was subcutaneously implanted into the right hind limb of BALB/c mice to establish a 4T1 tumor-bearing model. The 4T1 mice models were randomly divided into four groups: PBS, PBS + laser, AuNC@Bi_2Se_3 and AuNC@Bi_2Se_3 + laser ($n = 5$ per group) after 7 days. These mice were then intravenously injected with corresponding solutions (3 mg kg^{-1}) when the tumors had grown to an average volume of approximately 100 mm^3. After 8 h post-injection, PBS + laser and AuNC@Bi_2Se_3 + laser groups received NIR irradiation (808 nm, 1 W cm^{-2}, 10 min). The body weight and tumor volume of the mice were recorded during the treatment process, with the tumor volume calculated as (length × $width^2$)/2. The mice were euthanized after 18 days of treatment, and their main organs, blood, and tumor tissues were collected for more analysis. The animal study protocol was approved by the Animal Ethics Committee at The Second People's Hospital of Shenzhen (protocol code 20240099). All experimental procedures were conducted by institutional guidelines for the care and use of laboratory animals and protocols, which were approved by the Animal Care and Use Committee of Shenzhen Second People's Hospital, Shenzhen, Guangdong, 518035, China.

2.12 Biosafety

The main organs, including the heart, liver, spleen, lung, and kidney, were used for the preparation of biosafety detection. Hematoxylin/eosin (H&E) staining was performed for the histological examination of these organs following treatment with AuNC@Bi_2Se_3. The collected whole blood was analyzed for levels of alanine aminotransferase (ALT), aspartate aminotransferase (AST), blood urea nitrogen (BUN), total protein (TP), albumin (ALB), alkaline phosphatase (ALP), creatinine (CREA), and total bilirubin (TBIL) using an Automatic Biochemical Analyzer.

3. Results and discussions

3.1 Synthesis and characterizations

The fabrication of AuNC@Bi_2Se_3 is illustrated in Fig. 1. Briefly, Bi_2Se_3 nanosheets were prepared *via* the sonication-assisted liquid exfoliation process. AuNC@Bi_2Se_3 nanocomposites were synthesized by stirring the Au NCs aqueous solution with

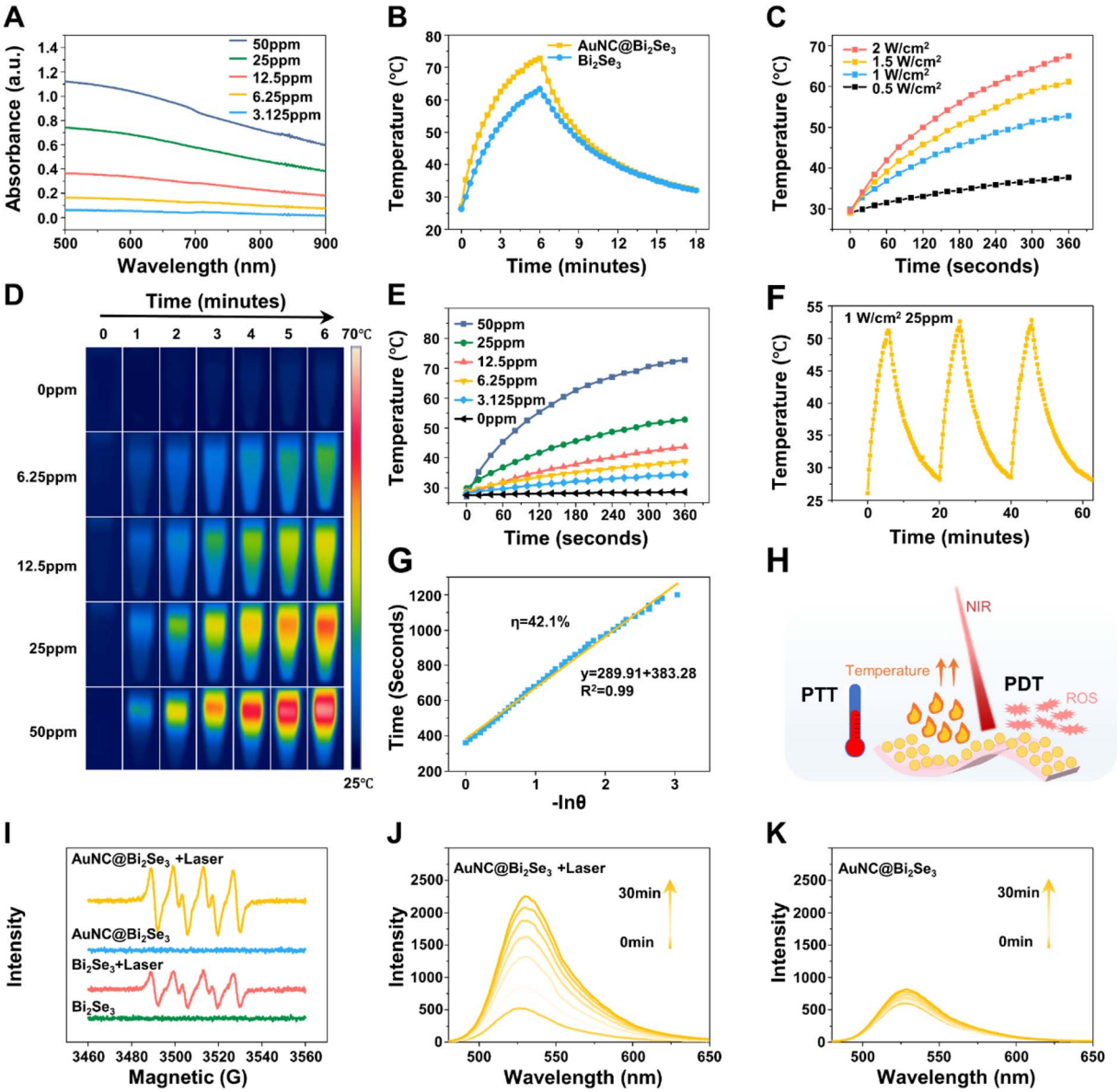

Fig. 3 (A) Absorbance spectra of AuNC@Bi_2Se_3 nanocomposites in different concentrations. (B) The photothermal heating curve of AuNC@Bi_2Se_3 and Bi_2Se_3 dispersions at 50 ppm. (C) The temperature curves of AuNC@Bi_2Se_3 at various power densities. (D) Thermal images of AuNC@Bi_2Se_3 solutions in different concentrations (0 ppm, 6.25 ppm, 12.5 ppm, 25 ppm, 50 ppm) under the irradiation of 808 nm laser (1 W cm^{-2}). (E) The temperature curves of AuNC@Bi_2Se_3 at various concentrations. (F) Temperature curve of AuNC@Bi_2Se_3 nanocomposites for three on/off cycles under 808 nm laser irradiation. (G) The calculation of PTCE. (H) Schematic representation of the anti-cancer mechanism involving AuNC@Bi_2Se_3 nanocomposites. (I) Electron spin resonance (ESR) spectra of four different groups to detect the production of $^{\bullet}O_2^-$ production. (J and K) $^{\bullet}O_2^-$ production of AuNC@Bi_2Se_3 with and without laser irradiation, respectively.

Bi_2Se_3 nanosheets at room temperature. Transmission electron microscopy (TEM) images indicated the morphology of AuNC@Bi_2Se_3 nanocomposites across different batches and showed their sheet-like structure (Fig. 2A and S1†). We can see in Fig. 2A that numerous AuNCs are uniformly distributed across the Bi_2Se_3 nanosheets' surface. What's more, the atomic force microscopy (AFM) images proved that the thickness of AuNC@Bi_2Se_3 nanocomposites was 6.59 nm which confirmed their 2D structure (Fig. S2†). High-resolution transmission electron microscopy (HRTEM) imaging and XRD patterns revealed that the hexagonal lattice fringes of the nanosheets have a distance of 0.207 nm, aligning with the (110) plane of the Bi_2Se_3 nanosheets crystal structure (Fig. 2B and S3†).[34] Additionally, we can see in Fig. 2B that the lattice fringe of the Au clusters was 0.235 nm, corresponding to the (111) plane of its face-centered cubic. The energy dispersive X-ray spectroscopy (EDX) analysis demonstrated that "Se", "Au" and "Bi" signals were detected in the AuNC@Bi_2Se_3 nanocomposites; whereas the copper peaks originated from the TEM grid. The metal ions distributed in single particles are 65.54, 0.34 and 34.13 weight percent of "Se", "Au" and "Bi", respectively, as seen in the inset of Fig. S3.† The elemental ratio in AuNC@Bi_2Se_3

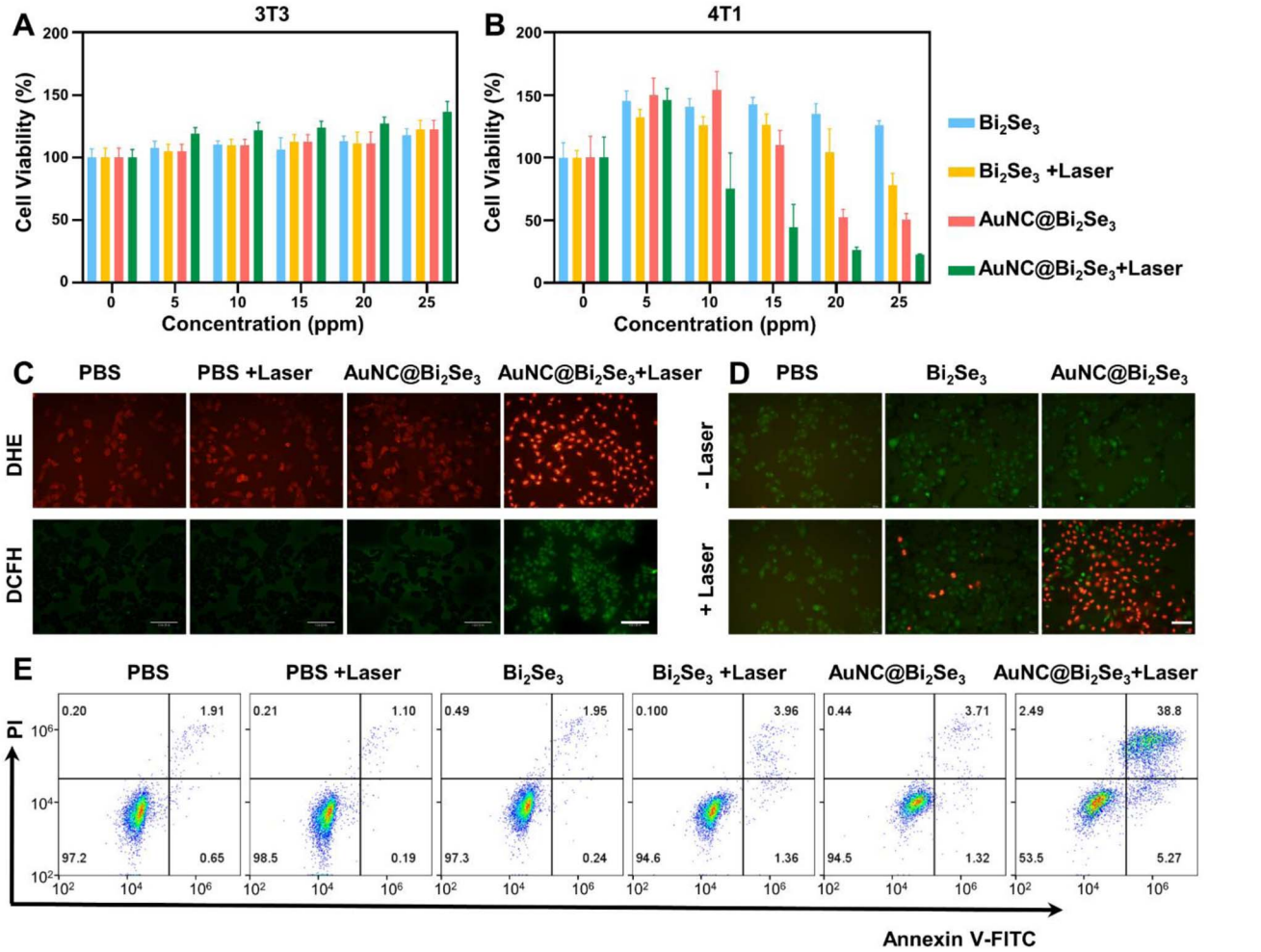

Fig. 4 (A) Cell viability of 3T3 cells and (B) 4T1 cells after incubation with various concentrations of AuNC@Bi_2Se_3 and Bi_2Se_3 nanocomposites. (C) 4T1 cells stained by DCFH and DHE in different groups (12.5 ppm), scale bar = 130 μm. (D) Calcein AM and propidium iodide (AM/PI) fluorescence images of 4T1 cells with different treatments (12.5 ppm), scale bar = 200 μm. (E) Flow cytometry of 4T1 cells induced in various treatments with annexin V-FITC/PI staining.

nanocomposites reveals the absence of Au peaks in the XRD spectrum. The high-angle annular dark-field scanning transmission electron microscopy (HAADF-STEM) image of AuNC@Bi_2Se_3 nanocomposites and their corresponding elemental mapping revealed the elemental composition of Au, Bi, and Se (Fig. 2C). The signals of Au elemental were captured in the outer layer, while Bi and Se elements were detected within, suggesting that Au clusters were distributed uniformly across the surface of the Bi_2Se_3 nanosheets (Fig. 2D). The images above suggested the successful synthesis of 2D AuNC@Bi_2Se_3 nanocomposites following the stirring process. The size of AuNC@Bi_2Se_3 nanocomposites and Bi_2Se_3 nanosheets was measured using dynamic light scattering (DLS). The average size of Bi_2Se_3 nanosheets was 171 nm (Fig. S4A†) while the particle diameter of AuNC@Bi_2Se_3 nanocomposites was approximately 146 nm which might be affected by the stirring process (Fig. 2E). The particle diameter of AuNC@Bi_2Se_3 nanocomposites with a well-distributed size range remained stable over 7 days, demonstrating their stability (Fig. S4B†). However, we still need to sonicate it for five minutes to avoid any potential complications before its utilization. Fig. 2F illustrates that the zeta potentials of Bi_2Se_3, Au NCs, and AuNC@Bi_2Se_3 were +40, −28, and +12 mV, respectively. The observed decrease in the zeta potential of AuNC@Bi_2Se_3 is attributed to the loading of the negatively charged Au NCs. Furthermore, the characterization of the synthesized AuNC@Bi_2Se_3 nanocomposites was detected by XPS. The full-scan XPS spectrum in Fig. 2G indicates that the hybrid nanomaterials are composed of Au, Bi, Se elements.[35] Fig. 2H illustrates the valence of Au 4f doublet of the obtained AuNC@Bi_2Se_3 nanocomposites. Two Au 4f peaks were observed at 84.2 and 87.9 eV, respectively, suggesting the presence of the Au^0 state.[36] Fig. 2I shows the peaks for Bi 4f at 157.4 and 162.7 eV, and Fig. 2J displays the broad peak of Se at 53.6 eV and 58.2 eV, which is assigned to the 3d level. These findings coherently indicate that the AuNC@Bi_2Se_3 nanocomposites were successfully fabricated.

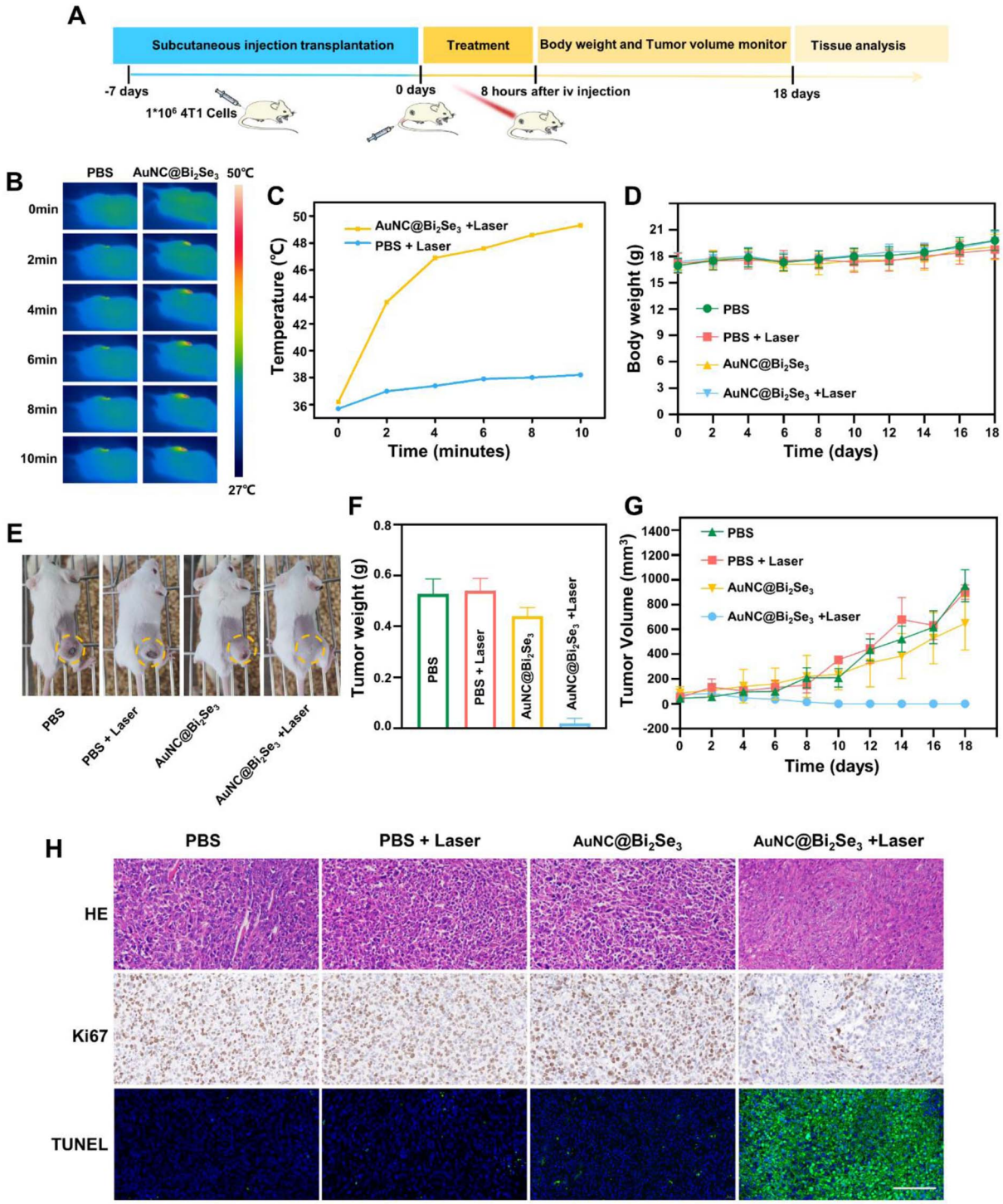

Fig. 5 (A) The treatment process of 4T1 tumor-bearing mice. (B) Thermal images after injection of PBS and AuNC@Bi_2Se_3 respectively and (C) their corresponding temperature curves under 808 nm laser irradiation. (D) The weight curves of 4T1 tumor-bearing mice. (E) Tumor photographs and (F) the excised tumor weights on the 18th day. (G) Their relative tumor growth curves in different groups in the treatment period. (H) H&E, Ki67 and TUNEL staining images of excised tumors of varying treatment groups on the 18th day. Scale bar = 100 μm.

3.2 Photothermal therapy

The ideal NIR absorption and exceptional PTCE of photothermal reagents are pivotal in PTT. Fig. 3A presents the visible-NIR absorbance spectra of AuNC@Bi_2Se_3 nanocomposites. The curves in the visible-NIR absorption spectrum revealed that AuNC@Bi_2Se_3 nanocomposites with different concentrations exhibit enhanced optical absorption in the 400–900 nm wavelength range. What's more, AuNC, Bi_2Se_3 nanosheets, and AuNC@Bi_2Se_3 nanocomposites collectively exhibit distinct

absorption peaks within the 800–900 nm wavelength range (Fig. S5†). Upon exposure to 808 nm near-infrared laser irradiation, the resonant frequency of the incident light coincides with the intrinsic frequency of the collective oscillation of free electrons during the LSPR effect, leading to maximal resonance intensity. This alignment results in a photothermal conversion efficacy of 808 nm laser irradiation surpassing that of 660 nm laser irradiation (Fig. S6†). Consequently, AuNC@Bi_2Se_3 nanocomposites showcased superior absorbance compared to Bi_2Se_3 nanosheets under the same concentration conditions (50 ppm), suggesting that the Au NCs play an important role in the improvement of the photothermal conversion capability of AuNC@Bi_2Se_3 nanocomposites (Fig. 3B and S5†). Under 808 nm laser irradiation (1.0 W cm^{-2}), the temperature of AuNC@Bi_2Se_3 nanocomposites raised depending on power density (Fig. 3C). Similarly, their temperature increases in a dose-dependent manner as the concentration is elevated. At a concentration of 3.125 ppm, the temperature rises from 28 to 34 °C in 6 minutes of irradiation, and further increases to 70 °C when the concentration is 50 ppm (Fig. 3D and E). In contrast, the thermal images of deionized water captured by the infrared camera shows no significant changes under the same conditions, indicating that AuNC@Bi_2Se_3 nanocomposites can convert NIR light into thermal energy efficiently. The photothermal stability of AuNC@Bi_2Se_3 was assessed by three recycling temperature variations of the AuNC@Bi_2Se_3 solution, with no significant reduction observed (Fig. 3F). This finding underscores the superior potential of AuNC@Bi_2Se_3 nanocomposites as PTAs for cancer treatment. According to calculations, the PTCE of AuNC@Bi_2Se_3 could reach up to 42.1% (Fig. 3G), significantly surpassing that of traditional 2D nanomaterials.[37–39] In summary, these results demonstrate that AuNC@Bi_2Se_3 nanomaterials possess exceptional photothermal conversion ability under 808 nm NIR laser irradiation, laying a solid foundation for future PTT applications.

3.3 Production of ROS

PDT is crucial in tumor therapy, and the generation of ROS is a key indicator of PDT effectiveness. Fig. 3H illustrates that AuNC@Bi_2Se_3 nanocomposites have both PTT and PDT effects. The ESR spectroscopy was used to evaluate the PDT capability of AuNC@Bi_2Se_3. As we can see in Fig. 3I and S7,† there are no obvious changes took place for the AuNC@Bi_2Se_3, Bi_2Se_3 and AuNC in a dark environment. However, all of them can generate ROS under NIR laser irradiation, with AuNC@Bi_2Se_3 generating more ROS than Bi_2Se_3 under the same concentration. To elucidate the enzymatic reaction mechanism of AuNC@Bi_2Se_3, we used DHR123 as a signal sensor for $^{\bullet}O_2^-$ to evaluate its PDT capability (Fig. 3J and K). After being irradiated for various minutes, the fluorescence value of AuNC@Bi_2Se_3 solution at 530 nm exhibited a significant upward trend, whereas the dark group showed no significant changes. These findings suggested that AuNC@Bi_2Se_3 nanocomposites can produce a substantial amount of ROS under 808 nm laser irradiation, demonstrating its effective PDT capability.

3.4 Intracellular ROS generation and cytotoxicity

The remarkable photothermal and photodynamic effects of AuNC@Bi_2Se_3 inspired us to investigate their cytotoxic effects on cancer cells. The *in vitro* anti-cancer effectiveness of AuNC@Bi_2Se_3 nanocomposites was assessed using the CCK8 assay. Initially, human normal cell lines, embryonic fibroblast cells (NIH 3T3), were utilized to access the biosafety of Bi_2Se_3 and AuNC@Bi_2Se_3 nanocomposites. As depicted in Fig. 4A, cell viability remained above 95% when the concentration was up to 25 ppm, confirming that there is no significant cytotoxicity of Bi_2Se_3 and AuNC@Bi_2Se_3 in human normal organs. However, within the simulated TME solutions enriched with excessive H_2O_2, a reduction in the viability of 4T1 cells is observed (Fig. 4B). In detail, the cell viability slightly decreased when treated with Bi_2Se_3 or AuNC@Bi_2Se_3 without NIR laser irradiation. After being irradiated by 808 nm laser for 5 minutes, nearly half of the cells were still alive when the concentration of Bi_2Se_3 was up to 25 ppm, whereas only 20% of cells were alive when treated with AuNC@Bi_2Se_3 under the same conditions. This finding demonstrates that the concentration and laser are major factors that affect cell toxicity and AuNC@Bi_2Se_3 exhibits higher efficiency in killing tumor cells under 808 nm laser irradiation. Furthermore, we examined the underlying cell death mechanism induced by AuNC@Bi_2Se_3 by assessing the cytotoxic ROS levels. As depicted in Fig. 4C, a significant production of ROS was observed in the group treated with 12.5 ppm AuNC@Bi_2Se_3 + laser, as indicated by DCFH-DA and DHE probes.[30,40] No green fluorescence was noted when treated with PBS, NIR laser, or AuNC@Bi_2Se_3 nanocomposites alone. However, strong green fluorescence was observed in 4T1 cells when an 808 nm laser was added to the 12.5 ppm AuNC@Bi_2Se_3 solution, indicating that AuNC@Bi_2Se_3 can efficiently generate ROS in the TME under laser irradiation, aligning with the results of cell experiments. Additionally, a DHE probe was used to detect intracellular $^{\bullet}O_2^-$. Different from the green fluorescence of DCFH-DA, red fluorescence can be detected in cells enriched with ROS by a DHE probe. As we can see, the group treated with 12.5 ppm AuNC@Bi_2Se_3 + laser showed obvious red fluorescence, while the group treated with PBS, PBS + laser, or AuNC@Bi_2Se_3 alone showed minimal fluorescence. The increased green and red fluorescence intensity in cells treated with AuNC@Bi_2Se_3 + laser exhibited positive generation of ROS and confirmed their superior photodynamic performance. The *in vitro* anti-cancer effect of AuNC@Bi_2Se_3 was directly visualized by fluorescence images of cells co-stained with fluorescent probes calcein AM (green fluorescence, representing live cells) and PI (red fluorescence, representing dead cells) (Fig. 4D). The cells treated with 12.5 ppm AuNC@Bi_2Se_3 + laser exhibited the most intense red fluorescence compared to other groups, confirming that AuNC@Bi_2Se_3 can cause significant cancer cell death under 808 nm laser irradiation. Additionally, the flow cytometry with annexin V-FITC/PI staining was employed to assess tumor cell apoptosis. The results in Fig. 4E indicated that the 12.5 ppm AuNC@Bi_2Se_3 nanocomposites can effectively induce 4T1 cell apoptosis *via* the irradiation of 808 nm laser. Collectively, these results fully demonstrated that AuNC@Bi_2Se_3

can efficiently increase the production of ROS and show extraordinary therapeutic efficiency for cancer cells.

3.5 *In vivo* anti-cancer effects of AuNC@Bi_2Se_3

Inspired by the outstanding *in vitro* photothermal effect of AuNC@Bi_2Se_3, we employed 4T1 tumor-bearing BALB/c mice model to evaluate their *in vivo* phototherapeutic effects. When the tumor volume reached approximately 100 mm^3, all the 4T1 tumor-bearing mice were divided into four groups ($n = 5$) at random: PBS, PBS + laser, AuNC@Bi_2Se_3, and AuNC@Bi_2Se_3 + laser and corresponding solutions were injected through tail intravenous injection (Fig. 5A). The infrared thermal camera was utilized to track heat signals, evaluating the *in vivo* thermal behaviors of AuNC@Bi_2Se_3 nanocomposites under the irradiation of an 808 nm laser (1 W cm^{-2}, 10 min). Zhang *et al.* reported that hyperthermia (temperatures higher than 42 °C) can achieve ideal tumor ablation.[41,42] We can see in the Fig. S8† that the temperature of PBS and AuNC@Bi_2Se_3 groups were decreased because of the inhalation of anesthetic gases, and PBS + laser group was around 37 °C with the help of 808 nm laser irradiation (Fig. 5B and C). However, the temperature on tumor regions in the AuNC@Bi_2Se_3 + laser group reached 49.3 °C, effectively ablating the tumor cells and inhibiting their malignant proliferation (Fig. 5B and C). Throughout the treatment process (18 days), the body weight of each group followed a similar trend (Fig. 5D), indicating that the treatment of AuNC@Bi_2Se_3 under 808 nm laser irradiation did not exhibit obvious systemic toxicity. Furthermore, the photographs and their corresponding tumor volumes of the 4T1 tumor-bearing mice after 18 days of treatment were illustrated in Fig. 5E–G. These results showed that the mice treated with AuNC@Bi_2Se_3 under 808 nm laser irradiation exhibited a sustainable decrease in tumor volume. In contrast, the tumor volumes of the other three groups did not exhibit any reduction during the treatment period. Additionally, the results from hematoxylin/eosin (H&E), TdT-mediated dUTP nick-end labeling (TUNEL), and Ki67 staining of tumor slices indicate that the group treated with AuNC@Bi_2Se_3 under NIR laser exposure displayed the highest rates of cell necrosis (Fig. 5H). Conversely, the groups treated with PBS, PBS + laser, or AuNC@Bi_2Se_3 alone showed no significant apoptosis or necrosis. These findings underscored that the AuNC@Bi_2Se_3 nanocomposites have superior photothermal efficacy and their anticancer activity is notably enhanced under 808 nm NIR laser irradiation.

3.6 *In vivo* biosafety evaluation

The biosafety of AuNC@Bi_2Se_3 nanocomposites is a critical prerequisite for their biomedical applications. Therefore, we assessed the biosafety of AuNC@Bi_2Se_3 nanocomposites in 4T1 tumor-bearing mice. Histological examinations of the heart, liver, lung, spleen and kidney were conducted using Hematoxylin & Eosin (H&E) staining. There were no significant histopathological lesions in mice treated with AuNC@Bi_2Se_3 or AuNC@Bi_2Se_3 + laser, compared to PBS and PBS + laser groups (Fig. S9†). The effects of these groups on blood functions were further examined by investigating ALT, AST (indicative of liver function), BUN (indicative of renal function), TP, ALB, ALP, TBIL, and CREA and the results indicated no significant differences among them (Fig. S10†). In summary, these findings demonstrate the excellent biosafety profile of AuNC@Bi_2Se_3 during the treatment period.

4. Conclusions

AuNC@Bi_2Se_3 nanocomposites were successfully fabricated using the sonication-assisted liquid exfoliation method and amide bond reaction. The photothermal conversion ability of AuNC@Bi_2Se_3 nanocomposites reached up to 42.1%, and their strong ability to produce ROS significantly enhances their killing efficiency on cancer cells. Furthermore, the AuNC@Bi_2Se_3 nanocomposites exhibited low toxicity but demonstrated efficient anticancer effects in both *in vitro* and *in vivo* therapeutic applications. Collectively, this work demonstrates that AuNC@Bi_2Se_3 nanocomposites are effective PTAs and PSs, suitable for synergistic PTT and PDT of cancer. We are confident that our strategy offers a valuable example for expanding the applications of Bi_2Se_3-based nanomaterials in biomedical fields.

Data availability

We confirm that the data supporting the findings of this study are available within the main article and ESI.†

Author contributions

Chenxi Li: investigation, methodology, data curation, formal analysis, writing—original draft; Xueyang Fang: writing—reviewing and editing, funding acquisition; Qingdong Zeng: investigation; Li Zeng: validation; Guohui Nie: funding acquisition and supervision; Bin Zhang: conceptualization, writing—reviewing and editing, funding acquisition. All authors read and approved the final manuscript.

Conflicts of interest

There are no conflicts to declare.

Acknowledgements

This work was financially supported by National Natural Science Foundation of China (52203335, 82192865 and 32301128), Shenzhen Science and Technology Innovation Committee (KCXFZ20201221173413038, JCYJ20210324103605014, ZDSYS201707281114196, LCYSSQ20220823091403007), Shenzhen Science and Technology Program (RCBS20221008093329063), Sanming Project of Medicine in Shenzhen (SZSM202211022), Shenzhen High-level Hospital Construction Fund, Development and Reform Commission of Shenzhen Municipality, Guangdong Basic and Applied Basic Research Foundation (2022A1515110803).

Notes and references

1 J. Liu, H. Dong, W. Wang, G. Wang, H. Pan, W. Chen, Q. Wang and Z.-J. Wang, *J. Clin. Oncol.*, 2021, **39**, e16002.
2 N. Abdallah, S. N. Patel, M. Nagasaka, S. Kim, H. E. Kim and A. Sukari, *J. Clin. Oncol.*, 2018, **36**, 207.
3 W.-D. Wang, Y.-Y. Guo, Z.-L. Yang, G.-L. Su and Z.-J. Sun, *ACS Nano*, 2023, **17**, 23262–23298.
4 X. Wu, Z. Zhou, K. Li and S. Liu, *Adv. Sci.*, 2024, 2308632.
5 R. Vankayala and K. C. Hwang, *Adv. Mater.*, 2018, **30**, 1706320.
6 Z. Xie, T. Fan, J. An, W. Choi, Y. Duo, Y. Ge, B. Zhang, G. Nie, N. Xie, T. Zheng, Y. Chen, H. Zhang and J. S. Kim, *Chem. Soc. Rev.*, 2020, **49**, 8065–8087.
7 M. Overchuk, R. A. Weersink, B. C. Wilson and G. Zheng, *ACS Nano*, 2023, **17**, 7979–8003.
8 Y. Wang, N. Gong, Y. Li, Q. Lu, X. Wang and J. Li, *J. Am. Chem. Soc.*, 2020, **142**, 1735–1739.
9 Z. Yang, D. Gao, J. Zhao, G. Yang, M. Guo, Y. Wang, X. Ren, J. S. Kim, L. Jin, Z. Tian and X. Zhang, *Nat. Rev. Clin. Oncol.*, 2023, **20**, 116–134.
10 W. Du, Y. Chong, X. Hu, Y. Wang, Y. Zhu, J. Chen, X. Li, Q. Zhang, G. Wang, J. Jiang and G. Liang, *Adv. Funct. Mater.*, 2020, **30**, 1908073.
11 X. He, Y. Hao, B. Chu, Y. Yang, A. Sun, K. Shi, C. Yang, K. Zhou, Y. Qu, H. Li and Z. Qian, *Nano Today*, 2021, **39**, 101174.
12 P. Dash, S. Thirumurugan, C.-L. Tseng, Y.-C. Lin, S.-L. Chen, U. Dhawan and R.-J. Chung, *ACS Appl. Mater. Interfaces*, 2023, **15**, 33335–33347.
13 Z. Zhou, J. Song, L. Nie and X. Chen, *Chem. Soc. Rev.*, 2016, **45**, 6597–6626.
14 M. Hayyan, M. A. Hashim and I. M. AlNashef, *Chem. Rev.*, 2016, **116**, 3029–3085.
15 C. Yee, W. Yang and S. Hekimi, *Cell*, 2014, **157**, 897–909.
16 L. Li, J. Fu, J. Ye, L. Liu, Z. Sun, H. Wang, S. Tan, M. Zhen, C. Wang and C. Bai, *Adv. Mater.*, 2024, 2310875.
17 D. Cen, Q. Zheng, B. Zheng, R. Zhou, X. Xiao, T. Zhang, Z. Huang, T. Yan, J. Yu, X. Li, R. Deng and X. Cai, *Adv. Funct. Mater.*, 2023, **33**, 2211402.
18 X. Yuan, B. Zhang, Z. Luo, Q. Yao, D. T. Leong, N. Yan and J. Xie, *Angew Chem. Int. Ed. Engl.*, 2014, **53**, 4623–4627.
19 S. Eustis and M. A. El-Sayed, *Chem. Soc. Rev.*, 2006, **35**, 209–217.
20 Y. Chen, L. Soler, C. Cazorla, J. Oliveras, N. G. Bastús, V. F. Puntes and J. Llorca, *Nat. Commun.*, 2023, **14**, 6165.
21 H. Yu, L. Xu, P. Wang, X. Wang and J. Yu, *Appl. Catal., B*, 2014, **144**, 75–82.
22 D. Jiang, Y. Zhang and X. Li, *Chin. J. Catal.*, 2019, **40**, 105–113.
23 C. Li, X. Fang, H. Zhang and B. Zhang, *Int. J. Nanomed.*, 2024, **19**, 805–824.
24 M.-Q. He, Y.-L. Yu and J.-H. Wang, *Nano Today*, 2020, **35**, 101005.
25 U. J. Kim, J. S. Kim, N. Park, S. Lee, U. Lee, Y. Park, J. Seok, S. Hwang, H. Son and Y. H. Lee, *ACS Nano*, 2018, **12**, 12733–12740.
26 O. Nicoletti, F. de la Peña, R. K. Leary, D. J. Holland, C. Ducati and P. A. Midgley, *Nature*, 2013, **502**, 80–84.
27 H. Xu, Y. Gu, S. Zhang, H. Xiong, F. Ma, F. Lu, Q. Ji, L. Liu, P. Ma, W. Hou, G. Yang and R. A. Lerner, *Angew. Chem., Int. Ed.*, 2020, **59**, 13663.
28 Y. Zhou, W. Feng, X. Qian, L. Yu, X. Han, G. Fan, Y. Chen and J. Zhu, *ACS Appl. Mater. Interfaces*, 2019, **11**, 19712–19723.
29 S. Zhao, R. Tian, B. Shao, Y. Feng, S. Yuan, L. Dong, L. Zhang, K. Liu, Z. Wang and H. You, *ACS Appl. Mater. Interfaces*, 2019, **11**, 394–402.
30 Z. Chu, T. Tian, Z. Tao, J. Yang, B. Chen, H. Chen, W. Wang, P. Yin, X. Xia, H. Wang and H. Qian, *Bioact. Mater.*, 2022, **17**, 71–80.
31 Z. Song, Y. Chang, H. Xie, X.-F. Yu, P. K. Chu and T. Chen, *NPG Asia Mater.*, 2017, **9**, e439.
32 Y. Nosaka and A. Y. Nosaka, *Chem. Rev.*, 2017, **117**, 11302–11336.
33 X. Fang, R. Gong, D. Yang, C. Li, Y. Zhang, Y. Wang, G. Nie, M. Li, X. Peng and B. Zhang, *J. Am. Chem. Soc.*, 2024, **146**, 15251–15263.
34 J. Yang, C. Wang, H. Ju, Y. Sun, S. Xing, J. Zhu and Q. Yang, *Adv. Funct. Mater.*, 2017, **27**, 1703864.
35 L. Xiao, A. Zhu, Q. Xu, Y. Chen, J. Xu and J. Weng, *ACS Appl. Mater. Interfaces*, 2017, **9**, 6931–6940.
36 F. Li, H. Yang, C. Shan, Q. Zhang, D. Han, A. Ivaska and L. Niu, *J. Mater. Chem.*, 2009, **19**, 4022–4025.
37 Z. Li, H. Zhang, J. Han, Y. Chen, H. Lin and T. Yang, *Adv. Mater.*, 2018, **30**, 1706981.
38 X. Fang, X. Wu, Z. Li, L. Jiang, W. S. Lo, G. Chen, Y. Gu and W. T. Wong, *Adv. Sci.*, 2020, **8**, 2003041.
39 X. Fang, D. Yang, X. Wu, K.-H. Lui, X. Li, W.-S. Lo, C. Li, Y. Zhang, G. Nie, L. Jiang, Y. Gu, B. Zhang and W.-T. Wong, *Chem. Eng. J.*, 2023, **474**, 145675.
40 C. Qi, J. He, L.-H. Fu, T. He, N. T. Blum, X. Yao, J. Lin and P. Huang, *ACS Nano*, 2021, **15**, 1627–1639.
41 X. Zhang, J. Du, Z. Guo, J. Yu, Q. Gao, W. Yin, S. Zhu, Z. Gu and Y. Zhao, *Adv. Sci.*, 2019, **6**, 1801122.
42 G. Kong, R. D. Braun and M. W. Dewhirst, *Cancer Res.*, 2001, **61**, 3027–3032.